NANO LETTERS

pubs.acs.org/NanoLett Letter

Synthesis, Magnetic Properties, and Electronic Structure of Magnetic Topological Insulator $MnBi_2Se_4$

Tiancong Zhu,[▽] Alexander J. Bishop,[▽] Tong Zhou, Menglin Zhu, Dante J. O'Hara, Alexander A. Baker, Shuyu Cheng, Robert C. Walko, Jacob J. Repicky, Tao Liu, Jay A. Gupta, Chris M. Jozwiak, Eli Rotenberg, Jinwoo Hwang, Igor Žutić, and Roland K. Kawakami*

Cite This: *Nano Lett.* 2021, 21, 5083−5090 Read Online

ACCESS | Metrics & More | Article Recommendations | Supporting Information

ABSTRACT: The intrinsic magnetic topological insulators $MnBi_2Te_4$ and $MnBi_2Se_4$ support novel topological states related to symmetry breaking by magnetic order. Unlike $MnBi_2Te_4$, the study of $MnBi_2Se_4$ has been inhibited by the lack of bulk crystals, as the van der Waals (vdW) crystal is not the thermodynamic equilibrium phase. Here, we report the layer-by-layer synthesis of vdW $MnBi_2Se_4$ crystals using nonequilibrium molecular beam epitaxy. Atomic-resolution scanning transmission electron microscopy and scanning tunneling microscopy identify a well-ordered vdW crystal with septuple-layer base units. The magnetic properties agree with the predicted layered antiferromagnetic ordering but disagree with its predicted out-of-plane orientation. Instead, our samples exhibit an easy-plane anisotropy, which is explained by including dipole−dipole interactions. Angle-resolved photoemission spectroscopy reveals the gapless Dirac-like surface state, which demonstrates that $MnBi_2Se_4$ is a topological insulator above the magnetic-ordering temperature. These studies show that $MnBi_2Se_4$ is a promising candidate for exploring rich topological phases of layered antiferromagnetic topological insulators.

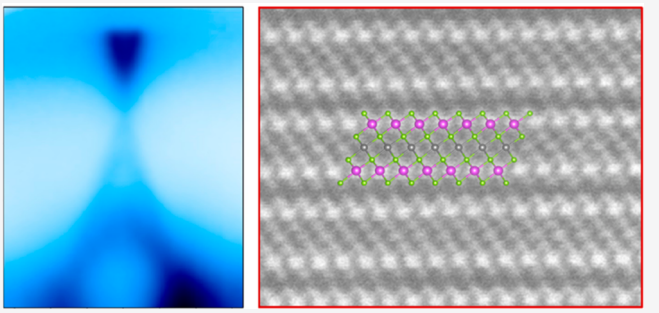

KEYWORDS: *Molecular beam epitaxy, magnetism, topological insulator, angle-resolved photoemission spectroscopy*

1. INTRODUCTION

The realization of novel topological quantum states is strongly correlated to the symmetries of different material systems.[1−3] In topological insulators (TIs), the existence of time reversal symmetry (TRS) yields a topologically protected gapless surface state distinguished from its gapped bulk states.[4−7] Breaking the TRS can lead to the quantum anomalous Hall (QAH) effect with dissipationless chiral edge states,[8−12] the axion insulator states with quantized magnetoelectric effects,[13−15] and Majorana fermions (by coupling to superconductors) obeying non-Abelian statistics.[16−18] Experimentally, the engineering of TRS in TIs has been achieved through doping the TIs with dilute transition metals (Cr, Mn, V, etc.),[19] where both QAH[20−22] and axion insulator states[23,24] have been observed at low temperature. However, one drawback of introducing magnetism through dilute doping is that the randomly distributed magnetic dopants can also induce disorder and nonuniformity in the sample, which ultimately limits QAH and axion insulator states from being realized at elevated temperatures.[25,26]

Consequently, researchers have increasingly focused on exploring intrinsic magnetic topological insulators, where the magnetic elements are ordered within the crystal lattice.[14] Among such systems, $MnBi_2X_4$ (X = Se, Te) has garnered substantial attention due to predictions of novel topological phases related to layered antiferromagnetic order.[27−31] These materials have a layered van der Waals (vdW) structure with covalently bonded septuple layers (SLs) (X−Bi−X−Mn−X−Bi−X) as the base unit (Figure 1a): essentially the magnetic Mn−X layer is inserted into each X−Bi−X−Bi−X layer of the corresponding TI. Although there have been experimental reports of axion insulator and QAH insulator phases in $MnBi_2Te_4$,[32,33] progress on topological phases in the selenide-based $MnBi_2Se_4$ has been limited by material synthesis. Efforts to synthesize bulk crystals have produced monoclinic $MnBi_2Se_4$ composed of magnetic chains,[34,35] its thermodynamically stable phase, as opposed to the desired vdW crystal. In addition, thin film growth has only produced isolated SLs within Bi_2Se_3[36] or at its surface,[37,38] while the synthesis of multilayer vdW $MnBi_2Se_4$ crystals needed for investigating interlayer magnetic coupling and topological effects has remained elusive.

Received: March 8, 2021
Revised: June 1, 2021
Published: June 7, 2021

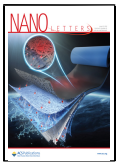

https://doi.org/10.1021/acs.nanolett.1c00141
Nano Lett. 2021, 21, 5083−5090

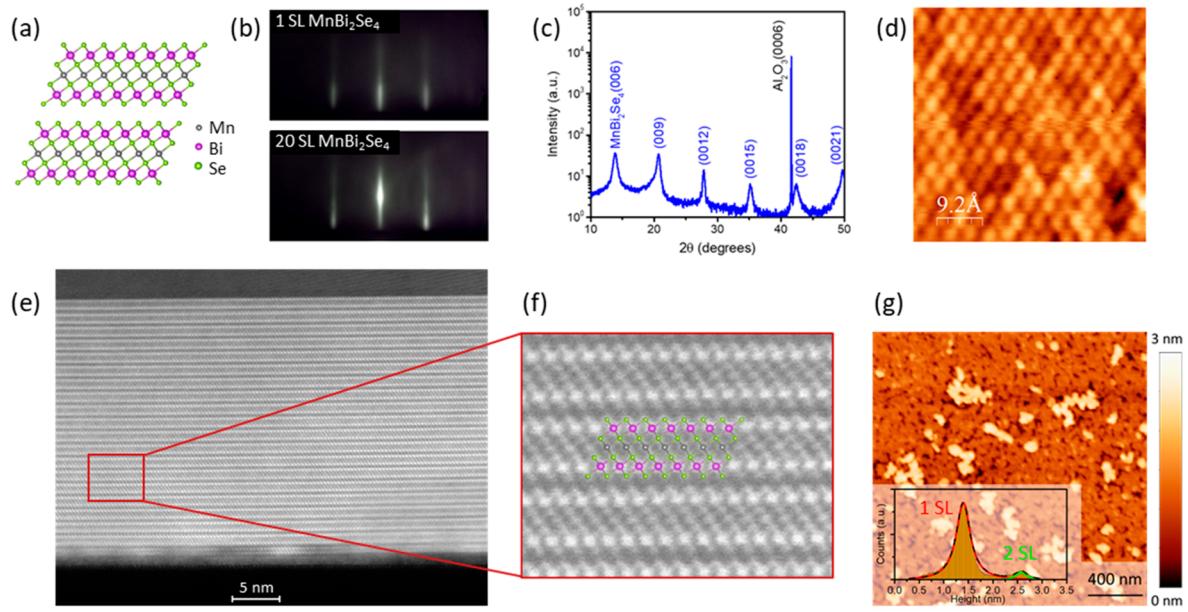

Figure 1. Structural characterization of $MnBi_2Se_4$ on $Al_2O_3(0001)$. (a) The atomic lattice structure of multilayer $MnBi_2Se_4$ consists of Se−Bi−Se−Mn−Se−Bi−Se septuple layers (SLs) in a van der Waals stack. (b) Streaky RHEED patterns on $MnBi_2Se_4$ films indicate a two-dimensional surface structure at thicknesses of 1 SL and 20 SL. (c) θ−2θ X-ray diffraction scans of a 20 SL $MnBi_2Se_4$ show that only the substrate ($Al_2O_3(0001)$) and the $MnBi_2Se_4(00l)$ planes are observed. (d) STM imaging reveals the atomic-scale surface structure of a 20 SL $MnBi_2Se_4$ film with a hexagonal surface structure and an in-plane lattice constant of 4.0 ± 0.1 Å. (e) Cross-sectional STEM imaging reveals the van der Waals stacking and atomic-scale structure of the film with the substrate on the bottom and an Se cap on the top. (f) Enlarged STEM image with atomic lattice overlay that matches with $MnBi_2Se_4$. (g) AFM images of a 1 SL film indicate a relatively flat film with regions of exposed substrate and the onset of second-layer nucleation. The height histogram (inset) shows the predominance of the monolayer film. The red and green solid lines show the Lorentzian fitting of the 1 SL and 2 SL profiles in the histogram, respectively, and the black dashed line shows the total fitting.

Here, we have successfully synthesized multilayer $MnBi_2Se_4$ vdW crystal films (up to 20 layers) using nonequilibrium molecular beam epitaxy (MBE) to stabilize the vdW layers and reveal their promising magnetic and topological properties. The atomic-scale structures have been verified by scanning transmission electron microscopy (STEM), scanning tunneling microscopy (STM), and atomic force microscopy (AFM). The magnetic properties have been investigated by superconducting quantum interference device (SQUID) magnetometry. A systematic study involving 10 samples of varying thicknesses reveal magnetic properties in agreement with the predicted layered antiferromagnetic ordering. On the other hand, the magnetic moments are found to lie in-plane, which disagrees with prior density functional theory (DFT) calculations predicting perpendicular magnetocrystalline anisotropy.[27,31,37] We reconcile this discrepancy by including the magnetic shape anisotropy (i.e., dipole−dipole interaction) in the magnetic anisotropy energy calculations, which leads to an overall magnetic anisotropy favoring in-plane orientation of the moments. The electronic band structure of $MnBi_2Se_4$ has been investigated by angle-resolved photoemission spectroscopy (ARPES) and DFT calculations. ARPES measurements of the paramagnetic phase reveal the presence of topological surface states with Dirac dispersion that lie within the bulk band gap, which demonstrates that $MnBi_2Se_4$ is a TI above the magnetic ordering temperature. Our initial study shows the promise of multilayer $MnBi_2Se_4$ for exploring the rich topological phases of layered antiferromagnetic TIs. These results also open new avenues of research into vdW heterostructures with the potential for achieving tunneling planar Hall effects, magnetic proximity effects,[39,40] and synthetic spin−orbit coupling.[41−46]

2. SYNTHESIS AND STRUCTURAL CHARACTERIZATION

Epitaxial $MnBi_2Se_4$ films are grown on $Al_2O_3(0001)$ substrates in a Veeco 930 MBE system (see section 1 in the Supporting Information for details). With the substrate held at 275 °C and under Se flux, we grow layers of $MnBi_2Se_4$ following a three-step process for each SL.[47] First, a quintuple layer of Bi_2Se_3 is grown by depositing the equivalent of two atomic layers of Bi. Next, we deposit a single atomic layer of Mn under Se flux and then wait for 5 min to allow the Mn to diffuse into the underlying Bi_2Se_3 template layer to form an individual trigonal $MnBi_2Se_4$ SL (Figure 1a). The reflection high energy electron diffraction (RHEED) images after each step can be found in Figures S2 and S3 of section 2 in the Supporting Information. This three-step process is repeated to create multilayer $MnBi_2Se_4$ to the desired thickness up to 20 SL, where sharp and streaky RHEED patterns persist throughout the growth (Figure 1b). The samples are typically capped with ∼10 nm amorphous Se before being removed from the MBE chamber for further characterization.

Various structural characterizations of the samples confirm the good crystalline quality of the material. θ−2θ X-ray diffraction measurements on a 20 SL sample show a series of peaks that correspond to the $MnBi_2Se_4(00l)$ planes (Figure 1c). These peaks yield an interplanar spacing of 12.76 Å in the sample, which is distinct from those of Bi_2Se_3 or other Mn−Se compounds. STM measurements on a 20 SL $MnBi_2Se_4$ sample (Figure 1d) reveal the hexagonal atomic structure of the sample surface consistent with imaging of the topmost Se layer, with an in-plane lattice constant of 4.0 ± 0.1 Å. Additional STM images are shown in section 3 in the Supporting Information. The crystal structure of the MBE-grown $MnBi_2Se_4$ is further investigated with cross-sectional STEM (see section 1 in the

https://doi.org/10.1021/acs.nanolett.1c00141
Nano Lett. 2021, 21, 5083−5090

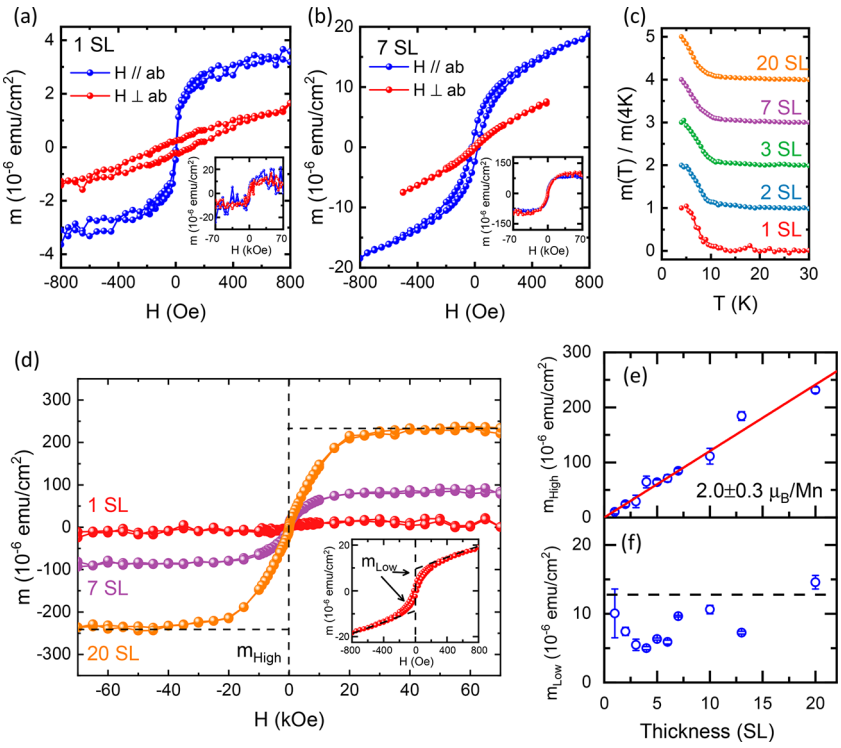

Figure 2. Magnetic properties of $MnBi_2Se_4$. (a) SQUID magnetization loops of a 1 SL $MnBi_2Se_4$ film at 4 K indicate ferromagnetic ordering with magnetic anisotropy favoring in-plane magnetization. The inset shows magnetization loops with higher field. (b) SQUID magnetization loops of a 7 SL $MnBi_2Se_4$ film at 4 K indicate ferromagnetic ordering with magnetic anisotropy favoring in-plane magnetization. The inset shows magnetization loops with higher field. (c) M vs T curves of $MnBi_2Se_4$ with different thicknesses shows a T_C value of ∼10 K. The curves are measured with a small applied field of 50 Oe. (d) A comparison of in-plane magnetization loops of 1, 7, and 20 SL films shows an increase in the saturation moment per area (m_{High}) with increasing thickness. All loops exhibit low-field hysteresis, where we define the extrapolated remanence (m_{Low}) as shown in the inset. (e) A linear dependence of m_{High} with film thickness is consistent with aligned magnetic moments in high field. (f) m_{Low} showing little variation with film thickness is consistent with a low-field antiferromagnetic state with net uncompensated moments or surface ferromagnetism. The dashed line marks the magnetic moment for 1 SL $MnBi_2Se_4$ based on 2.0 μ_B/Mn as determined by the slope in (e). Note: m_{Low} for the 1 SL sample in (f) is determined using the saturation value at high magnetic field (same method as m_{High}), due to no obvious hysteresis loop being observed at low field (a).

Supporting Information). The high-angle annular dark field (HAADF) image in Figure 1e shows the vdW stacking of SLs of the sample with a quintuple layer (QL) forming at the substrate (bottom), which might be associated with substrate preparation by Bi_2Se_3 growth and desorption[48] (see section 1 in the Supporting Information). The atomic structure of each SL in the enlarged image (Figure 1f) agrees very well with the trigonal $MnBi_2Se_4$ structure. The STEM measurement also confirms the continuous growth of multilayer $MnBi_2Se_4$ SLs, where previous studies have only shown isolated $MnBi_2Se_4$ layers within Bi_2Se_3 or at its surface.[36,37] Figure 1g shows the atomic force microscopy (AFM) measurements on a nominally single layer $MnBi_2Se_4$ sample (this sample is not capped with Se). The vast majority of the film is composed of monolayer regions, and a second layer has started to nucleate in some areas (bright regions). The height difference between the two regions is 11.8 ± 1.0 Å, which agrees well with the step height of $MnBi_2Se_4$. The AFM measurement on the 1 SL sample also confirms that the growth of $MnBi_2Se_4$ is dominated by the layer-by-layer growth mode, as opposed to three-dimensional islands, which is important for interpreting the magnetic properties in section 3. These structural characterizations confirm the high quality of the MBE-grown $MnBi_2Se_4$ films.

3. MAGNETIC PROPERTIES

A systematic study of magnetic properties with thicknesses varying from 1 to 20 SL (Figure 2) provides evidence for easy-plane magnetic anisotropy and layered antiferromagnetic order. Figure 2a shows the in-plane (blue) and out-of-plane (red) magnetization loops measured by SQUID at 4 K for a typical 1 SL sample. The in-plane loops exhibit a nonlinear ferromagnetic shape, while the out-of-plane loops are much flatter. These are signatures of ferromagnetism in the 1 SL sample with weak in-plane magnetic anisotropy. X-ray magnetic circular dichroism measurement on 1 SL samples further confirms that the magnetic signal originates from Mn atoms in our samples (section 4 in the Supporting Information). Similar ferromagnetic behavior is also observed for the 7 SL sample, as shown in Figure 2b, with a clearer hysteresis loop observed with in-plane measurement. Figure 2c shows the temperature dependence of the magnetization with a small in-plane field of 50 Oe for representative thicknesses (1, 2, 3, 7, 20 SL). With 4 K as the starting point, the magnetization decreases with increasing temperature and disappears at ∼10 K for all thicknesses. Figure 2d shows representative in-plane hysteresis loops for 1, 7, and 20 SL film thicknesses. The multilayer samples exhibit a ferromagnetic-like hysteresis at low fields (inset), as we discussed in Figure 2b. The associated magnetic moment, denoted m_{Low} (total moment per sample area), is extrapolated from M vs H curves where the hysteresis loop is closed, as indicated in the inset of Figure 2d. On the other hand, even though the hysteresis loop is closed above ∼500 Oe for the few-layer samples (e.g., Figure 2b), the measured magnetization does not saturate there. At higher fields, the magnetization gradually

https://doi.org/10.1021/acs.nanolett.1c00141
Nano Lett. 2021, 21, 5083−5090

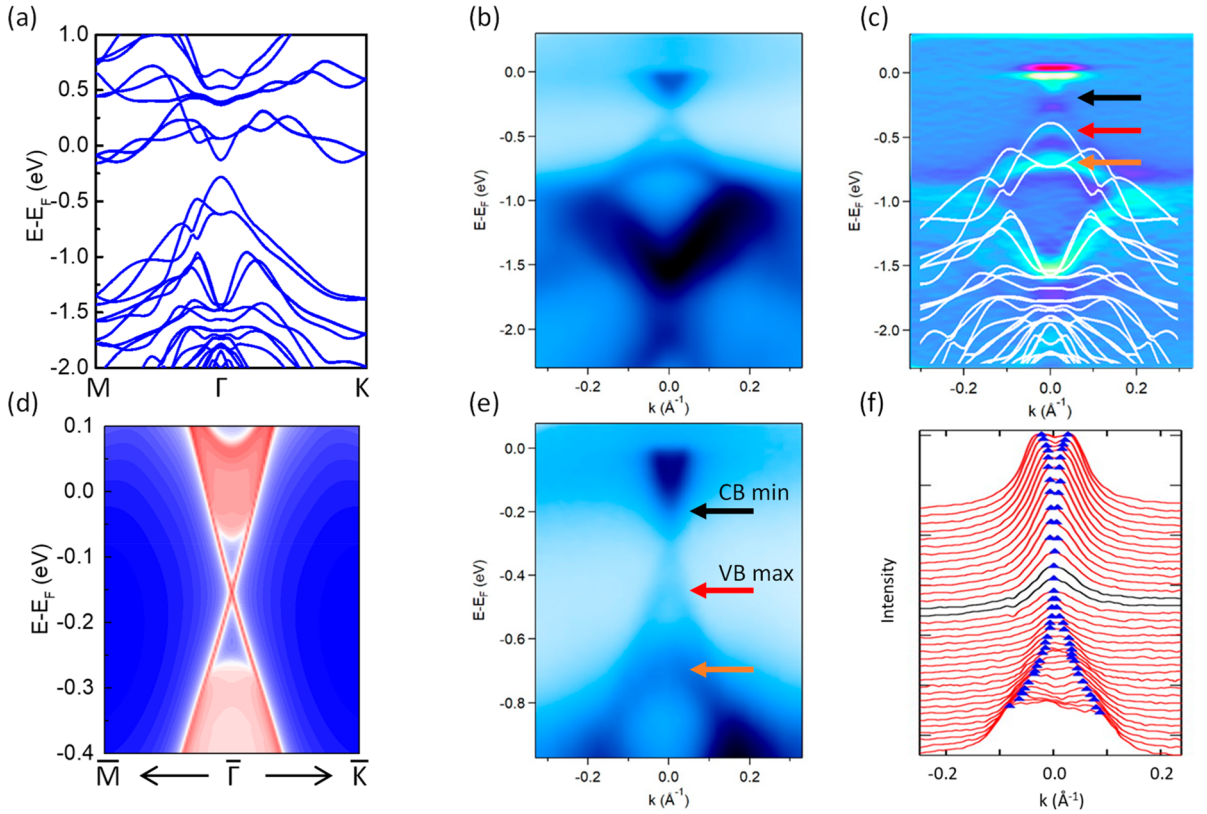

Figure 3. Electronic structure of $MnBi_2Se_4$. (a) DFT calculation of the bulk states with Mn treated as nonmagnetic. (b) ARPES measurement of a 7 SL $MnBi_2Se_4$ film along M−Γ−M with 20 eV photon energy and a sample temperature of 80 K. (c) An overlay of the DFT calculation and second derivative of the ARPES data in (b) shows a good agreement of calculation with the experiment. (d) DFT-calculated (001) surface states of nonmagnetic $MnBi_2Se_4$. (e) Enlarged view of the ARPES data that highlights the Dirac surface state. (f) A series of momentum distribution curves show the evolution of the Dirac cone for evenly spaced energies ranging from −0.75 eV (bottom curve) to 0.0 eV (top curve). Local maxima are indicated by blue triangles. Black curves indicate the Dirac point. For (c) and (e), the black arrows indicate the conduction band minimum, red arrows indicate the valence band maximum (faint band), and orange arrows indicate a lower valence band (prominent band).

increases until it finally saturates and the saturation magnetic moment is denoted as m_{High} (total moment per sample area). The values of m_{High} and m_{Low} across 10 samples of varying thicknesses are summarized in Figures 2e,f, respectively. The magnitude of m_{High} shows a linear dependence on film thickness, where the slope indicates a magnetic moment of 2.0 μ_B per Mn (Figure 2e). This is lower than the expected value of 5 μ_B/Mn for Mn^{2+} (S = 5/2). While the origin of the reduced moment is unclear, prior studies of reduced magnetic moments in $MnBi_2Te_4$, $MnBi_4Te_7$, and $MnBi_{2-x}Sb_xTe_4$ provide insight into this issue[49−56] (section 5 in the Supporting Information). In contrast to m_{High}, m_{Low} does not increase linearly with thickness and maintains a value of less than a monolayer of Mn (indicated by the dashed curve). Finally, transport measurements with features similar to those of the magnetic properties provide support that magnetic signals originate from the deposited films (section 6 in the Supporting Information).

The magnetic measurements are in agreement with DFT calculations[27,31] for $MnBi_2Se_4$ that predict intralayer ferromagnetic coupling and interlayer antiferromagnetic coupling for a layered antiferromagnetic state. The intralayer ferromagnetic exchange interaction is established by our magnetic measurement for the 1 SL sample that exhibits ferromagnetic behavior (Figure 2a). To address the interlayer antiferromagnetic coupling, we discuss the magnetism in few-layer $MnBi_2Se_4$. Although a ferromagnetic behavior is observed in few SL samples (Figure 2b), the magnetic moment associated with ferromagnetism (m_{Low}) is significantly different from the total saturation moment of the samples (m_{High}). This shows that few-SL samples are not simply ferromagnetic. When the scaling of m_{High} and m_{Low} is compared with thickness (Figure 2e,f), the saturation moment m_{High} increases linearly with thickness, while m_{Low} does not vary much with thickness. This further rules out the scenario where the ferromagnetic signal is from random doping of Mn atoms, in which case m_{Low} should also scale with thickness (i.e., the amount of Mn deposition). Finally, by fitting the data in Figure 2e, we find the slope of 12.7 ± 1.9 emu/cm^2 per SL corresponds to 2.0 ± 0.3 μ_B per Mn. Comparing this with the data in Figure 2f, we find that all of the m_{Low} values are within the magnetization of 1 SL $MnBi_2Se_4$. All this evidence is consistent with layered antiferromagnetism with weak interlayer coupling. Under a low magnetic field, the Zeeman energy is weak in comparison to the interlayer AFM coupling; thus, the sample remains antiferromagnetic. However, due to the presence of monolayer thickness fluctuation (Figure 1g), certain regions of the few-layer $MnBi_2Se_4$ can have an odd number of layers where the magnetic moments are not compensated by antiferromagnetic ordering. As a result, a ferromagnetic-like feature with a total moment below the 1 SL value is observed. Under high magnetic field, the Zeeman energy can overcome the interlayer AFM coupling. In this case, all of the magnetic moments are aligned with the external field and, as a result, the total magnetic moment is scaled with film thickness.

https://doi.org/10.1021/acs.nanolett.1c00141
Nano Lett. 2021, 21, 5083−5090

The weak strength of interlayer AFM coupling is evidenced by the weak thickness dependence of the magnetic transition temperature. This can be understood in the mean-field picture. In a mean-field analysis, the ordering temperature T_C will be proportional to $z_F|J_F| + z_{AF}|J_{AF}|$, where z_F (z_{AF}) is the number of nearest neighbors and J_F (J_{AF}) is the ferromagnetic (antiferromagnetic) exchange coupling constant for moments in the same (neighboring) SL. In the limit of $|J_F| \gg |J_{AF}|$, the T_C value will be dominated by the ferromagnetic exchange. As a result, T_C should be insensitive to sample thickness, as is observed experimentally. While mean-field theory does not properly take dimensionality or fluctuations into account, it nevertheless shows how the two different exchange couplings contribute to a single magnetic phase transition and explains the negligible variation of T_C with thickness (Figure 2c) due to the dominance of J_F over J_{AF}.

Finally, we discuss the observed in-plane magnetic anisotropy in our $MnBi_2Se_4$ films. This is in apparent disagreement with previous DFT calculations of the magnetocrystalline anisotropy (MCA) in $MnBi_2Se_4$ that predict perpendicular magnetic anisotropy (PMA).[27,31,37] To resolve this discrepancy, we calculated the magnetic anisotropy energy (MAE) including both the MCA and magnetic shape anisotropy (i.e., dipolar interactions) (see section 7 in the Supporting Information for details). Our calculations find that, while the MCA does exhibit PMA, its strength is sufficiently low that the inclusion of magnetic shape anisotropy yields an overall magnetic anisotropy favoring in-plane orientation of the moments.

4. ELECTRONIC STRUCTURE AND TOPOLOGICAL SURFACE STATES

We investigate the electronic and topological properties by performing ARPES measurements (see section 1 in the Supporting Information) on a 7 SL $MnBi_2Se_4$ film and compare them with DFT calculations. The ARPES measurements are performed at 80 K, where the sample is paramagnetically ordered. Simulating the paramagnetic order using DFT calculations is challenging. However, a nonmagnetic case can be a good approximation to capture the key electronic structure at the Γ point of the paramagnetic case, which has been verified in the similar system $MnBi_2Te_4$.[57] Thus, we calculate the bands of a nonmagnetic $MnBi_2Se_4$ crystal as shown in Figure 3a. The key message here is the topological property of the bands at the Γ point. The calculated topological invariant Z_2 of 1 shows a nontrivial gap of ∼0.2 eV at the Γ point, indicating that gapless Dirac surface states exist in the $MnBi_2Se_4$ surface and confirmed by the surface state calculation. To investigate the nature of these surface states, we perform DFT calculations on a semi-infinite slab of $MnBi_2Se_4$. The calculation confirms the presence of a topological surface state with Dirac dispersion (red lines in Figure 3d) in addition to the bulk states, which appear as the solid red regions of Figure 3d in a projection onto the (001) plane.

Figure 3b shows the energy−momentum relation along the M−Γ−M direction measured by ARPES (other cuts are shown in section 8 in the Supporting Information), which agrees well with the DFT calculation. To obtain a reliable identification of the bulk bands, we overlay the DFT calculation with the experimental data (Figure 3c), where we have taken the second derivative of the ARPES data along the energy axis to improve the contrast of the energy bands. The excellent overlap of the DFT calculation with the experimental spectra provides a confident assignment of the bulk conduction and valence bands. On the basis of this assignment of bands, we identify the positions of the conduction band (CB) minimum (black arrow) and valence band (VB) maximum (red arrow) in the ARPES spectra.

The existence of a Dirac-like surface state in nonmagnetic $MnBi_2Se_4$ is clearly observed in enlarged ARPES spectra (Figure 3e), where the linearly dispersing bands are connecting the CB minimum (black arrow) and VB maximum (red arrow) of $MnBi_2Se_4$. The bulk gap in ARPES (∼0.25 eV in Figure 3e) is similar to that of the DFT calculation (∼0.20 eV in Figure 3d). To investigate the surface state in the experimental data, we plot the momentum distribution curves for a series of energies that traverse the bulk band gap (Figure 3f). We observe a crossing of the local maxima (indicated by the blue triangles), which signifies the Dirac point and the gapless nature of the surface state within our energy resolution. Energy distribution curves (section 8 in the Supporting Information) further corroborate the gapless nature of the surface state.

5. DISCUSSION

It is worthwhile to compare our results to prior studies of related materials. Previous studies of Mn-doped Bi_2Se_3 reported in-plane ferromagnetism with $T_C \approx 10$ K, similar to our findings.[58−60] Subsequent TEM studies of Mn-doped Bi_2Se_3 by Hagmann et al.[36] revealed the self-assembly of isolated $MnBi_2Se_4$ layers within Bi_2Se_3, leading the authors to propose a re-evaluation of the origin of ferromagnetism in the previous studies. Our results further support this viewpoint, where the linear thickness dependence of the saturation moment (Figure 2e) and the direct visualization of $MnBi_2Se_4$ (Figure 1) indicate that our magnetic signals originate from $MnBi_2Se_4$ layers. In addition, we exclude the possibility of magnetic signals from dilute Mn doping of Bi_2Se_3 by growing directly on the Al_2O_3 substrates without a Bi_2Se_3 buffer layer. Thus, the similar magnetic ordering temperatures suggest $MnBi_2Se_4$ layers as a common origin of the magnetic signals.

Another study by Hirahara et al.[37] investigated the magnetic properties and band structure of a monolayer of $MnBi_2Se_4$ on Bi_2Se_3. The results showed room-temperature ferromagnetism with perpendicular moments and the opening of a gap in the Bi_2Se_3 surface state. The magnetic properties are quite different from those of our current study but are similar to those of a recent study of epitaxial $MnSe_2$ films showing room-temperature ferromagnetism and perpendicular hysteresis.[61] Further, the growth procedure developed in this paper is different from that of the earlier work, so it may be that the materials themselves are different. For instance, we have found in STM studies that the growth of $MnSe_2$ onto Bi_2Se_3 produces islands with different step heights and that these are sensitive to the growth conditions.[62] A notable distinction of the present study is the ability to grow multilayer $MnBi_2Se_4$ as verified by STEM, which allows us to confidently ascribe the T_C value of ∼10 K to multilayer $MnBi_2Se_4$. Additional studies would be needed to reconcile the differences in the monolayer limit.

6. CONCLUSIONS

We have developed the MBE synthesis of multilayer trigonal $MnBi_2Se_4$, a material that does not exist in bulk crystal form. STEM and STM imaging confirms the high quality of the material and identifies the atomic-scale structure of the septuple layer—the building block of the van der Waals crystal. Magnetic measurements indicate that the single-layer $MnBi_2Se_4$ is

https://doi.org/10.1021/acs.nanolett.1c00141
Nano Lett. 2021, 21, 5083−5090

ferromagnetic with a Curie temperature of ∼10 K. The thickness-dependent magnetic properties agree with layered antiferromagnetic order. The observed magnetic properties, including the unexpected in-plane easy plane, are explained by DFT studies that include magnetocrystalline and magnetic shape anisotropy. These calculations along with ARPES measurements confirm the presence of a topological Dirac surface state, revealing that $MnBi_2Se_4$ in the paramagnetic state is a topological insulator. Our findings indicate the discovery of an intrinsically magnetic TI which could prove useful in future research endeavors.

With the realization of this high-quality magnetic TI we expect several interesting directions for future research in van der Waals heterostructures. In the normal state, magnetic TI/TI heterostructures could enable a peculiar tunneling planar Hall effect, which attains its maximum signal for the in-plane magnetization along the current direction, when the usual planar and other Hall effects vanish.[41,42] In the superconducting heterostructures, such magnetic TIs could provide both magnetic proximity effects and synthetic spin−orbit coupling through magnetic textures to support spin-triplet superconductivity, an important element for superconducting spintronics[43,44] and tunable Majorana bound states.[42,45,46]

7. METHODS

See section 1 in the Supporting Information.

■ ASSOCIATED CONTENT

Supporting Information

The Supporting Information is available free of charge at https://pubs.acs.org/doi/10.1021/acs.nanolett.1c00141.

Methods (MBE, STEM, XMCD, ARPES, DFT), evolution of RHEED images during growth, additional STM images, XMCD data, discussion of the reduced magnetic moment, transport measurements, magnetic anisotropy calculations, and additional ARPES data (PDF)

■ AUTHOR INFORMATION

Corresponding Author

Roland K. Kawakami − *Department of Physics, The Ohio State University, Columbus, Ohio 43210, United States;* orcid.org/0000-0003-0245-9192; Email: kawakami.15@osu.edu

Authors

Tiancong Zhu − *Department of Physics, The Ohio State University, Columbus, Ohio 43210, United States;* orcid.org/0000-0003-2703-5652

Alexander J. Bishop − *Department of Physics, The Ohio State University, Columbus, Ohio 43210, United States*

Tong Zhou − *Department of Physics, University at Buffalo, Buffalo, New York 14260, United States*

Menglin Zhu − *Department of Materials Science and Engineering, The Ohio State University, Columbus, Ohio 43210, United States*

Dante J. O'Hara − *Department of Physics, The Ohio State University, Columbus, Ohio 43210, United States; Materials Science and Engineering, University of California, Riverside, California 92521, United States*

Alexander A. Baker − *Lawrence Livermore National Laboratory, Livermore, California 94550, United States;* orcid.org/0000-0003-0700-0858

Shuyu Cheng − *Department of Physics, The Ohio State University, Columbus, Ohio 43210, United States*

Robert C. Walko − *Department of Physics, The Ohio State University, Columbus, Ohio 43210, United States*

Jacob J. Repicky − *Department of Physics, The Ohio State University, Columbus, Ohio 43210, United States*

Tao Liu − *Department of Physics, The Ohio State University, Columbus, Ohio 43210, United States*

Jay A. Gupta − *Department of Physics, The Ohio State University, Columbus, Ohio 43210, United States*

Chris M. Jozwiak − *Advanced Light Source, Lawrence Berkeley National Laboratory, Berkeley, California 94720, United States;* orcid.org/0000-0002-0980-3753

Eli Rotenberg − *Advanced Light Source, Lawrence Berkeley National Laboratory, Berkeley, California 94720, United States;* orcid.org/0000-0002-3979-8844

Jinwoo Hwang − *Department of Materials Science and Engineering, The Ohio State University, Columbus, Ohio 43210, United States*

Igor Žutić − *Department of Physics, University at Buffalo, Buffalo, New York 14260, United States*

Complete contact information is available at: https://pubs.acs.org/10.1021/acs.nanolett.1c00141

Author Contributions

$^{\nabla}$T.Z. and A.J.B. contributed equally.

Author Contributions

R.K.K. and T.Zhu conceived the study. T.Zhu and A.J.B. synthesized the material with the help of D.J.O. T.Zhu performed the magnetometry measurement and data analysis with the help of A.J.B. and D.J.O. T.L. and T.Zhu performed the transport measurements. M.Z. performed the STEM measurement. T.Zhu and R.C.W. performed the STM measurement with the help of J.J.R. D.J.O. and A.A.B. performed the XMCD measurement. T.Zhu, A.J.B., S.C., and R.K.K. performed the ARPES measurements with C.M.J. and E.R. T.Zhou and I.Z. performed DFT calculations and theoretical analysis. All authors contributed to the interpretation of the results and preparation of the manuscript.

Notes

The authors declare no competing financial interest.

■ ACKNOWLEDGMENTS

We thank J. Freeland and J.-B. Forien for support with the XMCD measurements, M. R. Brenner for support with the MBE growth, and A. Bostwick and R. A. Bennett for assistance with the ARPES measurements. We thank Yusheng Hou for helpful discussions about the MAE calculations. This work was primarily supported by the Department of Energy (DOE) Basic Energy Sciences under Grant No. DE-SC0016379. A.J.B. and R.K.K. acknowledge support from AFOSR MURI 2D MAGIC (FA9550-19-1-0390). Part of this work was performed under the auspices of the U.S. DOE by Lawrence Livermore National Laboratory (LLNL) under Contract No. DE-AC52-07NA27344 and was supported by the LLNL-LDRD program under Project No. 19-LW-028. Portions of this work were performed at Sector 4 of the APS, Argonne National Laboratory. The APS is a U.S. DOE Office of Science User Facility operated for the DOE Office of Science by ANL under Contract No. DE-

AC02-06CH11357. This research used resources of the Advanced Light Source, a DOE Office of Science User Facility under Contract no. DE-AC02-05CH11231. M.Z. and J.H. acknowledge partial support from the Center for Emergent Materials, an NSF MRSEC, under Grant No. DMR-2011876. T.Zhou and I.Z. were supported by U.S. DOE Office of Science, Basic Energy Sciences, under Grant No. DE-SC0004890 and the UB Center for Computational Research.

REFERENCES

(1) Hasan, M. Z.; Kane, C. L. Colloquium: Topological insulators. *Rev. Mod. Phys.* **2010**, *82*, 3045−3067.
(2) Moore, J. E. The birth of topological insulators. *Nature* **2010**, *464*, 194−198.
(3) Qi, X.-L.; Zhang, S.-C. Topological insulators and superconductors. *Rev. Mod. Phys.* **2011**, *83*, 1057−1110.
(4) Chen, Y. L.; Analytis, J. G.; Chu, J.-H.; Liu, Z. K.; Mo, S.-K.; Qi, X. L.; Zhang, H. J.; Lu, D. H.; Dai, X.; Fang, Z.; Zhang, S. C.; Fisher, I. R.; Hussain, Z.; Shen, Z.-X. Experimental Realization of a Three-Dimensional Topological Insulator, Bi_2Te_3. *Science* **2009**, *325*, 178−181.
(5) Hsieh, D.; Qian, D.; Wray, L.; Xia, Y.; Hor, Y. S.; Cava, R. J.; Hasan, M. Z. A topological Dirac insulator in a quantum spin Hall phase. *Nature* **2008**, *452*, 970−974.
(6) Zhang, T.; Cheng, P.; Chen, X.; Jia, J.-F.; Ma, X.; He, K.; Wang, L.; Zhang, H.; Dai, X.; Fang, Z.; Xie, X.; Xue, Q.-K. Experimental Demonstration of Topological Surface States Protected by Time-Reversal Symmetry. *Phys. Rev. Lett.* **2009**, *103*, 266803.
(7) Hsieh, D.; Xia, Y.; Qian, D.; Wray, L.; Meier, F.; Dil, J. H.; Osterwalder, J.; Patthey, L.; Fedorov, A. V.; Lin, H.; Bansil, A.; Grauer, D.; Hor, Y. S.; Cava, R. J.; Hasan, M. Z. Observation of Time-Reversal-Protected Single-Dirac-Cone Topological-Insulator States in Bi_2Te_3 and Sb_2Te_3. *Phys. Rev. Lett.* **2009**, *103*, 146401.
(8) Qi, X.-L.; Wu, Y.-S.; Zhang, S.-C. Topological quantization of the spin Hall effect in two-dimensional paramagnetic semiconductors. *Phys. Rev. B: Condens. Matter Mater. Phys.* **2006**, *74*, 085308.
(9) Liu, C.-X.; Qi, X.-L.; Dai, X.; Fang, Z.; Zhang, S.-C. Quantum Anomalous Hall Effect in $Hg_{1-y}Mn_yTe$ Quantum Wells. *Phys. Rev. Lett.* **2008**, *101*, 146802.
(10) Nomura, K.; Nagaosa, N. Surface-Quantized Anomalous Hall Current and the Magnetoelectric Effect in Magnetically Disordered Topological Insulators. *Phys. Rev. Lett.* **2011**, *106*, 166802.
(11) Yu, R.; Zhang, W.; Zhang, H.-J.; Zhang, S.-C.; Dai, X.; Fang, Z. Quantized Anomalous Hall Effect in Magnetic Topological Insulators. *Science* **2010**, *329*, 61−64.
(12) Qi, X.-L.; Hughes, T. L.; Zhang, S.-C. Topological field theory of time-reversal invariant insulators. *Phys. Rev. B: Condens. Matter Mater. Phys.* **2008**, *78*, 195424.
(13) Essin, A. M.; Moore, J. E.; Vanderbilt, D. Magnetoelectric Polarizability and Axion Electrodynamics in Crystalline Insulators. *Phys. Rev. Lett.* **2009**, *102*, 146805.
(14) Mong, R. S. K.; Essin, A. M.; Moore, J. E. Antiferromagnetic topological insulators. *Phys. Rev. B: Condens. Matter Mater. Phys.* **2010**, *81*, 245209.
(15) Li, R.; Wang, J.; Qi, X.-L.; Zhang, S.-C. Dynamical axion field in topological magnetic insulators. *Nat. Phys.* **2010**, *6*, 284−288.
(16) Lian, B.; Wang, J.; Zhang, S.-C. Edge-state-induced Andreev oscillation in quantum anomalous Hall insulator-superconductor junctions. *Phys. Rev. B: Condens. Matter Mater. Phys.* **2016**, *93*, 161401.
(17) Wang, J.; Zhou, Q.; Lian, B.; Zhang, S.-C. Chiral topological superconductor and half-integer conductance plateau from quantum anomalous Hall plateau transition. *Phys. Rev. B: Condens. Matter Mater. Phys.* **2015**, *92*, 064520.
(18) Qi, X.-L.; Hughes, T. L.; Zhang, S.-C. Chiral topological superconductor from the quantum Hall state. *Phys. Rev. B: Condens. Matter Mater. Phys.* **2010**, *82*, 184516.
(19) Tokura, Y.; Yasuda, K.; Tsukazaki, A. Magnetic topological insulators. *Nat. Rev. Phys.* **2019**, *1*, 126−143.
(20) Chang, C.-Z.; Zhang, J.; Feng, X.; Shen, J.; Zhang, Z.; Guo, M.; Li, K.; Ou, Y.; Wei, P.; Wang, L.-L.; Ji, Z.-Q.; Feng, Y.; Ji, S.; Chen, X.; Jia, J.; Dai, X.; Fang, Z.; Zhang, S.-C.; He, K.; Wang, Y.; Lu, L.; Ma, X.-C.; Xue, Q.-K. Experimental Observation of the Quantum Anomalous Hall Effect in a Magnetic Topological Insulator. *Science* **2013**, *340*, 167−170.
(21) Checkelsky, J. G.; Yoshimi, R.; Tsukazaki, A.; Takahashi, K. S.; Kozuka, Y.; Falson, J.; Kawasaki, M.; Tokura, Y. Trajectory of the anomalous Hall effect towards the quantized state in a ferromagnetic topological insulator. *Nat. Phys.* **2014**, *10*, 731−736.
(22) Kou, X.; Guo, S.-T.; Fan, Y.; Pan, L.; Lang, M.; Jiang, Y.; Shao, Q.; Nie, T.; Murata, K.; Tang, J.; Wang, Y.; He, L.; Lee, T.-K.; Lee, W.-L.; Wang, K. L. Scale-Invariant Quantum Anomalous Hall Effect in Magnetic Topological Insulators beyond the Two-Dimensional Limit. *Phys. Rev. Lett.* **2014**, *113*, 137201.
(23) Mogi, M.; Kawamura, M.; Yoshimi, R.; Tsukazaki, A.; Kozuka, Y.; Shirakawa, N.; Takahashi, K. S.; Kawasaki, M.; Tokura, Y. A magnetic heterostructure of topological insulators as a candidate for an axion insulator. *Nat. Mater.* **2017**, *16*, 516−521.
(24) Xiao, D.; Jiang, J.; Shin, J.-H.; Wang, W.; Wang, F.; Zhao, Y.-F.; Liu, C.; Wu, W.; Chan, M. H. W.; Samarth, N.; Chang, C.-Z. Realization of the Axion Insulator State in Quantum Anomalous Hall Sandwich Heterostructures. *Phys. Rev. Lett.* **2018**, *120*, 056801.
(25) Lee, I.; Kim, C. K.; Lee, J.; Billinge, S. J. L.; Zhong, R.; Schneeloch, J. A.; Liu, T.; Valla, T.; Tranquada, J. M.; Gu, G.; Davis, J. C. S. Imaging Dirac-mass disorder from magnetic dopant atoms in the ferromagnetic topological insulator $Cr_x(Bi_{0.1}Sb_{0.9})_{2-x}Te_3$. *Proc. Natl. Acad. Sci. U. S. A.* **2015**, *112*, 1316−1321.
(26) Wang, W.; Yang, F.; Gao, C.; Jia, J.; Gu, G. D.; Wu, W. Visualizing ferromagnetic domains in magnetic topological insulators. *APL Mater.* **2015**, *3*, 083301.
(27) Chowdhury, S.; Garrity, K. F.; Tavazza, F. Prediction of Weyl semimetal and antiferromagnetic topological insulator phases in Bi_2MnSe_4. *Npj Comput. Mater.* **2019**, *5*, 33.
(28) Otrokov, M. M.; Rusinov, I. P.; Blanco-Rey, M.; Hoffmann, M.; Vyazovskaya, A. Y.; Eremeev, S. V.; Ernst, A.; Echenique, P. M.; Arnau, A.; Chulkov, E. V. Unique Thickness-Dependent Properties of the van der Waals Interlayer Antiferromagnet $MnBi_2Te_4$ Films. *Phys. Rev. Lett.* **2019**, *122*, 107202.
(29) Li, J.; Li, Y.; Du, S.; Wang, Z.; Gu, B.-L.; Zhang, S.-C.; He, K.; Duan, W.; Xu, Y. Intrinsic magnetic topological insulators in van der Waals layered $MnBi_2Te_4$-family materials. *Sci. Adv.* **2019**, *5*, No. eaaw5685.
(30) Zhang, D.; Shi, M.; Zhu, T.; Xing, D.; Zhang, H.; Wang, J. Topological Axion States in the Magnetic Insulator $MnBi_2Te_4$ with the Quantized Magnetoelectric Effect. *Phys. Rev. Lett.* **2019**, *122*, 206401.
(31) Zhang, H.; Yang, W.; Wang, Y.; Xu, X. Tunable topological states in layered magnetic materials of $MnSb_2Te_4$, $MnBi_2Se_4$, and $MnSb_2Se_4$. *Phys. Rev. B: Condens. Matter Mater. Phys.* **2021**, *103*, 094433.
(32) Liu, C.; Wang, Y.; Li, H.; Wu, Y.; Li, Y.; Li, J.; He, K.; Xu, Y.; Zhang, J.; Wang, Y. Robust axion insulator and Chern insulator phases in a two-dimensional antiferromagnetic topological insulator. *Nat. Mater.* **2020**, *19*, 522−527.
(33) Deng, Y.; Yu, Y.; Shi, M. Z.; Guo, Z.; Xu, Z.; Wang, J.; Chen, X. H.; Zhang, Y. Quantum anomalous Hall effect in intrinsic magnetic topological insulator $MnBi_2Te_4$. *Science* **2020**, *367*, 895−900.
(34) Ranmohotti, K. G. S.; Djieutedjeu, H.; Poudeu, P. F. P. Chemical Manipulation of Magnetic Ordering in $Mn_{1-x}Sn_xBi_2Se_4$ Solid-Solutions. *J. Am. Chem. Soc.* **2012**, *134*, 14033−14042.
(35) Nowka, C.; Gellesch, M.; Enrique Hamann Borrero, J.; Partzsch, S.; Wuttke, C.; Steckel, F.; Hess, C.; Wolter, A. U. B.; Teresa Corredor Bohorquez, L.; Büchner, B.; Hampel, S. Chemical vapor transport and characterization of $MnBi_2Se_4$. *J. Cryst. Growth* **2017**, *459*, 81−86.
(36) Hagmann, J. A.; Li, X.; Chowdhury, S.; Dong, S.-N.; Rouvimov, S.; Pookpanratana, S. J.; Man Yu, K.; Orlova, T. A.; Bolin, T. B.; Segre, C. U.; Seiler, D. G.; Richter, C. A.; Liu, X.; Dobrowolska, M.; Furdyna, J. K. Molecular beam epitaxy growth and structure of self-assembled Bi_2Se_3/Bi_2MnSe_4 multilayer heterostructures. *New J. Phys.* **2017**, *19*, 085002.

https://doi.org/10.1021/acs.nanolett.1c00141
Nano Lett. 2021, 21, 5083−5090

(37) Hirahara, T.; Eremeev, S. V.; Shirasawa, T.; Okuyama, Y.; Kubo, T.; Nakanishi, R.; Akiyama, R.; Takayama, A.; Hajiri, T.; Ideta, S.-i.; Matsunami, M.; Sumida, K.; Miyamoto, K.; Takagi, Y.; Tanaka, K.; Okuda, T.; Yokoyama, T.; Kimura, S.-i.; Hasegawa, S.; Chulkov, E. V. Large-Gap Magnetic Topological Heterostructure Formed by Subsurface Incorporation of a Ferromagnetic Layer. *Nano Lett.* **2017**, *17*, 3493−3500.
(38) Okuyama, Y.; Ishikawa, R.; Kuroda, S.; Hirahara, T. Role of hybridization and magnetic effects in massive Dirac cones: Magnetic topological heterostructures with controlled film thickness. *Appl. Phys. Lett.* **2019**, *114*, 051602.
(39) Žutić, I.; Matos-Abiague, A.; Scharf, B.; Dery, H.; Belashchenko, K. Proximitized materials. *Mater. Today* **2019**, *22*, 85−107.
(40) Xu, J.; Singh, S.; Katoch, J.; Wu, G.; Zhu, T.; Zutic, I.; Kawakami, R. K. Spin inversion in graphene spin valves by gate-tunable magnetic proximity effect at one-dimensional contacts. *Nat. Commun.* **2018**, *9*, 2869.
(41) Tang, H. X.; Kawakami, R. K.; Awschalom, D. D.; Roukes, M. L. Giant Planar Hall Effect in Epitaxial (Ga,Mn)As Devices. *Phys. Rev. Lett.* **2003**, *90*, 107201.
(42) Fatin, G. L.; Matos-Abiague, A.; Scharf, B.; Žutić, I. Wireless Majorana Bound States: From Magnetic Tunability to Braiding. *Phys. Rev. Lett.* **2016**, *117*, 077002.
(43) Linder, J.; Robinson, J. W. A. Superconducting spintronics. *Nat. Phys.* **2015**, *11*, 307−315.
(44) Martínez, I.; Högl, P.; González-Ruano, C.; Cascales, J. P.; Tiusan, C.; Lu, Y.; Hehn, M.; Matos-Abiague, A.; Fabian, J.; Žutić, I.; Aliev, F. G. Interfacial Spin-Orbit Coupling: A Platform for Superconducting Spintronics. *Phys. Rev. Appl.* **2020**, *13*, 014030.
(45) Zhou, T.; Mohanta, N.; Han, J. E.; Matos-Abiague, A.; Žutić, I. Tunable magnetic textures in spin valves: From spintronics to Majorana bound states. *Phys. Rev. B: Condens. Matter Mater. Phys.* **2019**, *99*, 134505.
(46) Desjardins, M. M.; Contamin, L. C.; Delbecq, M. R.; Dartiailh, M. C.; Bruhat, L. E.; Cubaynes, T.; Viennot, J. J.; Mallet, F.; Rohart, S.; Thiaville, A.; Cottet, A.; Kontos, T. Synthetic spin-orbit interaction for Majorana devices. *Nat. Mater.* **2019**, *18*, 1060−1064.
(47) Gong, Y.; Guo, J.; Li, J.; Zhu, K.; Liao, M.; Liu, X.; Zhang, Q.; Gu, L.; Tang, L.; Feng, X.; Zhang, D.; Li, W.; Song, C.; Wang, L.; Yu, P.; Chen, X.; Wang, Y.; Yao, H.; Duan, W.; Xu, Y.; Zhang, S.-C.; Ma, X.; Xue, Q.-K.; He, K. Experimental Realization of an Intrinsic Magnetic Topological Insulator. *Chin. Phys. Lett.* **2019**, *36*, 076801.
(48) Levy, I.; Garcia, T. A.; Shafique, S.; Tamargo, M. C. Reduced twinning and surface roughness of Bi_2Se_3 and Bi_2Te_3 layers grown by molecular beam epitaxy on sapphire substrates. *J. Vac. Sci. Technol., B: Nanotechnol. Microelectron.: Mater., Process., Meas., Phenom.* **2018**, *36*, 02D107.
(49) Yan, J. Q.; Okamoto, S.; McGuire, M. A.; May, A. F.; McQueeney, R. J.; Sales, B. C. Evolution of structural, magnetic, and transport properties in $MnBi_{2-x}Sb_xTe_4$. *Phys. Rev. B: Condens. Matter Mater. Phys.* **2019**, *100*, 104409.
(50) Chen, B.; Fei, F.; Zhang, D.; Zhang, B.; Liu, W.; Zhang, S.; Wang, P.; Wei, B.; Zhang, Y.; Zuo, Z.; Guo, J.; Liu, Q.; Wang, Z.; Wu, X.; Zong, J.; Xie, X.; Chen, W.; Sun, Z.; Wang, S.; Zhang, Y.; Zhang, M.; Wang, X.; Song, F.; Zhang, H.; Shen, D.; Wang, B. Intrinsic magnetic topological insulator phases in the Sb doped $MnBi_2Te_4$ bulks and thin flakes. *Nat. Commun.* **2019**, *10*, 4469.
(51) Hu, C.; Gordon, K. N.; Liu, P.; Liu, J.; Zhou, X.; Hao, P.; Narayan, D.; Emmanouilidou, E.; Sun, H.; Liu, Y.; Brawer, H.; Ramirez, A. P.; Ding, L.; Cao, H.; Liu, Q.; Dessau, D.; Ni, N. A van der Waals antiferromagnetic topological insulator with weak interlayer magnetic coupling. *Nat. Commun.* **2020**, *11*, 97.
(52) Vidal, R. C.; Zeugner, A.; Facio, J. I.; Ray, R.; Haghighi, M. H.; Wolter, A. U. B.; Corredor Bohorquez, L. T.; Caglieris, F.; Moser, S.; Figgemeier, T.; Peixoto, T. R. F.; Vasili, H. B.; Valvidares, M.; Jung, S.; Cacho, C.; Alfonsov, A.; Mehlawat, K.; Kataev, V.; Hess, C.; Richter, M.; Büchner, B.; van den Brink, J.; Ruck, M.; Reinert, F.; Bentmann, H.; Isaeva, A. Topological Electronic Structure and Intrinsic Magnetization in $MnBi_4Te_7$: A Bi_2Te_3 Derivative with a Periodic Mn Sublattice. *Phys. Rev. X* **2019**, *9*, 041065.
(53) Ding, L.; Hu, C.; Ye, F.; Feng, E.; Ni, N.; Cao, H. Crystal and magnetic structures of magnetic topological insulators $MnBi_2Te_4$ and $MnBi_4Te_7$. *Phys. Rev. B: Condens. Matter Mater. Phys.* **2020**, *101*, 020412.
(54) Zeugner, A.; Nietschke, F.; Wolter, A. U. B.; Gaß, S.; Vidal, R. C.; Peixoto, T. R. F.; Pohl, D.; Damm, C.; Lubk, A.; Hentrich, R.; Moser, S. K.; Fornari, C.; Min, C. H.; Schatz, S.; Kißner, K.; Ünzelmann, M.; Kaiser, M.; Scaravaggi, F.; Rellinghaus, B.; Nielsch, K.; Hess, C.; Büchner, B.; Reinert, F.; Bentmann, H.; Oeckler, O.; Doert, T.; Ruck, M.; Isaeva, A. Chemical Aspects of the Candidate Antiferromagnetic Topological Insulator $MnBi_2Te_4$. *Chem. Mater.* **2019**, *31*, 2795−2806.
(55) Lee, S. H.; Zhu, Y.; Wang, Y.; Miao, L.; Pillsbury, T.; Yi, H.; Kempinger, S.; Hu, J.; Heikes, C. A.; Quarterman, P.; Ratcliff, W.; Borchers, J. A.; Zhang, H.; Ke, X.; Graf, D.; Alem, N.; Chang, C.-Z.; Samarth, N.; Mao, Z. Spin scattering and noncollinear spin structure-induced intrinsic anomalous Hall effect in antiferromagnetic topological insulator $MnBi_2Te_4$. *Phys. Rev. Research* **2019**, *1*, 012011.
(56) Yan, J. Q.; Zhang, Q.; Heitmann, T.; Huang, Z.; Chen, K. Y.; Cheng, J. G.; Wu, W.; Vaknin, D.; Sales, B. C.; McQueeney, R. J. Crystal growth and magnetic structure of $MnBi_2Te_4$. *Physical Review Materials* **2019**, *3*, 064202.
(57) Hao, Y.-J.; Liu, P.; Feng, Y.; Ma, X.-M.; Schwier, E. F.; Arita, M.; Kumar, S.; Hu, C.; Lu, R. e.; Zeng, M.; Wang, Y.; Hao, Z.; Sun, H.-Y.; Zhang, K.; Mei, J.; Ni, N.; Wu, L.; Shimada, K.; Chen, C.; Liu, Q.; Liu, C. Gapless Surface Dirac Cone in Antiferromagnetic Topological Insulator $MnBi_2Te_4$. *Phys. Rev. X* **2019**, *9*, 041038.
(58) Zhang, D.; Richardella, A.; Rench, D. W.; Xu, S.-Y.; Kandala, A.; Flanagan, T. C.; Beidenkopf, H.; Yeats, A. L.; Buckley, B. B.; Klimov, P. V.; Awschalom, D. D.; Yazdani, A.; Schiffer, P.; Hasan, M. Z.; Samarth, N. Interplay between ferromagnetism, surface states, and quantum corrections in a magnetically doped topological insulator. *Phys. Rev. B: Condens. Matter Mater. Phys.* **2012**, *86*, 205127.
(59) von Bardeleben, H. J.; Cantin, J. L.; Zhang, D. M.; Richardella, A.; Rench, D. W.; Samarth, N.; Borchers, J. A. Ferromagnetism in Bi_2Se_3:Mn epitaxial layers. *Phys. Rev. B: Condens. Matter Mater. Phys.* **2013**, *88*, 075149.
(60) Tarasenko, R.; Vališka, M.; Vondráček, M.; Horáková, K.; Tkáč, V.; Carva, K.; Baláž, P.; Holý, V.; Springholz, G.; Sechovský, V.; Honolka, J. Magnetic and structural properties of Mn-doped Bi2Se3 topological insulators. *Phys. B* **2016**, *481*, 262−267.
(61) O'Hara, D. J.; Zhu, T.; Trout, A. H.; Ahmed, A. S.; Luo, Y. K.; Lee, C. H.; Brenner, M. R.; Rajan, S.; Gupta, J. A.; McComb, D. W.; Kawakami, R. K. Room Temperature Intrinsic Ferromagnetism in Epitaxial Manganese Selenide Films in the Monolayer Limit. *Nano Lett.* **2018**, *18*, 3125−3131.
(62) Noesges, B. A.; Zhu, T.; Repicky, J. J.; Yu, S.; Yang, F.; Gupta, J. A.; Kawakami, R. K.; Brillson, L. J. Chemical migration and dipole formation at van der Waals interfaces between magnetic transition metal chalcogenides and topological insulators. *Physical Review Materials* **2020**, *4*, 054001.

https://doi.org/10.1021/acs.nanolett.1c00141
Nano Lett. 2021, 21, 5083−5090